Icarus 302 (2018) 285–295

Contents lists available at ScienceDirect

Icarus

journal homepage: www.elsevier.com/locate/icarus

Amorphous salts formed from rapid dehydration of multicomponent chloride and ferric sulfate brines: Implications for Mars

Elizabeth C. Sklute[a,*], A. Deanne Rogers[b], Jason C. Gregerson[b], Heidi B. Jensen[b,1], Richard J. Reeder[b], M. Darby Dyar[a]

[a] Department of Astronomy, Mount Holyoke College, 50 College St., South Hadley, MA 01075, USA
[b] Department of Geoscience, Stony Brook University, 255 Earth and Space Science Building, Stony Brook, NY 11794-2100, USA

ARTICLE INFO

Article history:
Received 19 May 2017
Revised 4 October 2017
Accepted 17 November 2017
Available online 21 November 2017

ABSTRACT

Salts with high hydration states have the potential to maintain high levels of relative humidity (RH) in the near subsurface of Mars, even at moderate temperatures. These conditions could promote deliquescence of lower hydrates of ferric sulfate, chlorides, and other salts. Previous work on deliquesced ferric sulfates has shown that when these materials undergo rapid dehydration, such as that which would occur upon exposure to present day Martian surface conditions, an amorphous phase forms. However, the fate of deliquesced halides or mixed ferric sulfate-bearing brines are presently unknown. Here we present results of rapid dehydration experiments on Ca–, Na–, Mg– and Fe–chloride brines and multicomponent ($Fe_2(SO_4)_3 \pm$ Ca, Na, Mg, Fe, Cl, HCO_3) brines at ~21 °C, and characterize the dehydration products using visible/near-infrared (VNIR) reflectance spectroscopy, mid-infrared attenuated total reflectance spectroscopy, and X-ray diffraction (XRD) analysis. We find that rapid dehydration of many multicomponent brines can form amorphous solids or solids with an amorphous component, and that the presence of other elements affects the persistence of the amorphous phase under RH fluctuations. Of the pure chloride brines, only Fe–chloride formed an amorphous solid. XRD patterns of the multicomponent amorphous salts show changes in position, shape, and magnitude of the characteristic diffuse scattering observed in all amorphous materials that could be used to help constrain the composition of the amorphous salt. Amorphous salts deliquesce at lower RH values compared to their crystalline counterparts, opening up the possibility of their role in potential deliquescence-related geologic phenomena such as recurring slope lineae (RSLs) or soil induration. This work suggests that a wide range of aqueous mixed salt solutions can lead to the formation of amorphous salts and are possible for Mars; detailed studies of the formation mechanisms, stability and transformation behaviors of amorphous salts are necessary to further constrain their contribution to Martian surface materials.

1. Introduction

Orbital and landed instruments at Mars have provided significant advances in our understanding of Martian surface materials, as well as a number of new questions and enigmatic observations. For example, the Mars Science Laboratory CheMin instrument (Bish et al., 2013), which contains an X-ray diffractometer, has detected X-ray amorphous (hereafter, "amorphous") materials in every soil and rock measurement thus far, with abundance estimates ranging from ~15–75 wt% (e.g., Blake et al., 2012; Blake et al., 2013; Treiman et al., 2016; Yen et al., 2017). Supporting measurements from the APXS and SAM instruments have constrained the bulk chemistry (including S and Cl) and hydrated nature of the amorphous fraction (Leshin et al., 2013; McAdam et al., 2014; Dehouck et al., 2015; Morris et al., 2015a); however, in general, the phase(s) that comprise this fraction are poorly constrained. A variety or combination of phases are plausible, including volcanic glasses, allophane (Morris et al., 2013), hisingerite (Milliken and Bish, 2014), amorphous sulfate (Sklute et al., 2015; Dehouck et al., 2014), chemisorbed sulfate on nanophase materials (McAdam et al., 2014; Rampe et al., 2016), or other nanophases (e.g., Dehouck et al., 2016). Important steps toward constraining the composition(s) of the constituents of the amorphous fraction include determining the possible formation mechanisms of amorphous materials, their stability under Martian conditions (e.g., Dehouck et al., 2016), and their spectral and X-ray diffraction characteristics.

* Corresponding author.
E-mail address: ecsklute@mtholyoke.edu (E.C. Sklute).
[1] Current address: 2354 Antiqua Court, Reston, VA 20191, USA.

https://doi.org/10.1016/j.icarus.2017.11.018
0019-1035/

Amorphous salts represent a potential component of Martian soils, but thus far have received little attention. In this work, we first review previous laboratory studies in which amorphous salt was reported, and describe known pathways under which amorphous salts form (Section 2). Next, we present methods for brine dehydration using chloride and multicomponent solutions (Section 3). X-ray diffraction (XRD), visible/near-infrared (VNIR) reflectance, and mid-infrared (MIR) attenuated total reflectance (ATR) data for the brine dehydration products are shown in Section 4. Last, we discuss potential implications related to the formation and persistence of amorphous salts on the Martian surface and subsurface (Sections 5 and 6).

2. Background

The body of literature describing the formation and stability of amorphous salts is relatively small, usually with amorphous phases reported as an intermediate or final run product of experiments designed to explore phase transitions as a function of temperature (T), relative humidity (RH), or precipitation rate. Generally, there are two broad pathways through which amorphous salts have been shown to form: (1) rapid dehydration of crystalline hydrates or (2) direct precipitation from brines, under non-equilibrium conditions. Higher crystalline hydrates ($>6H_2O$ per sulfate) of Mg- or Fe(II)-sulfate exposed to vacuum will form an amorphous phase through rapid dehydration (Vaniman et al., 2004; Wang et al., 2006; Chipera and Vaniman, 2007; Wang et al., 2009, 2011, 2012, 2013; Sklute et al., 2015). However, the rate of dehydration and amorphization from a crystalline starting material is temperature dependent (Wang et al., 2009, 2013). For example, vacuum desiccation of epsomite leads to an amorphous phase within two hours at 21 °C, but at −8 °C, an amorphous phase was not observed, even after ~200 h at that temperature (Wang et al., 2009). It is not clear whether amorphization would occur over longer timescales at cold temperatures.

Direct precipitation of amorphous salts from brines usually requires rapid (non-equilibrium) precipitation, driven by liquid instability and/or supersaturation (e.g., Franks, 1993). For example, amorphous ferric sulfate solids were produced from rapid dehydration of ferric sulfate brines, either by decreasing RH or decreasing atmospheric pressure (Xu et al., 2009; Xu and Parise, 2012; Sklute et al., 2015). Rapid precipitation has also been accomplished through cryoprecipitation, wherein liquids become quickly supersaturated through a rapid decrease in temperature (Toner et al., 2014; Morris et al., 2015b). In kinetic precipitation experiments of CO_2-supersaturated Ca–Mg–Fe–H_2O solutions at low-temperatures (~25 °C) and neutral pH, amorphous Fe-rich carbonate phases were early precipitates (Golden et al., 2000). For Na- and Mg-perchlorates, brine supersaturation achieved by cooling the liquid below the eutectic temperature (supercooling) has also been shown to yield amorphous phases (Toner et al., 2014). Toner et al. (2014) suggested that brine viscosity is a major factor in whether a salt glass forms via supercooling, and speculated that viscous ferric sulfate brines would show similar behavior to perchlorates.

These findings raise several questions, such as: Do other, pure component brines (such as chloride brines) or multi-component brines form amorphous solids upon rapid dehydration? How do additional elements in ferric sulfate brines affect the stability of the dehydration product to RH fluctuations? What are the IR spectral properties and XRD characteristics of these amorphous products? To that end, we conducted a series of experiments to investigate the rapid dehydration products of chloride and multicomponent (ferric sulfate; iron-, magnesium-, and calcium-, and sodium-chloride; and sodium bicarbonate) brines. These brine compositions were chosen because calculations of the Martian amorphous composition (e.g., Morris et al., 2016, 2015a; Rampe et al., 2017; Treiman et al., 2016; Yen et al., 2017) demonstrate that Fe^{2+}, Fe^{3+}, Mg^{2+}, Ca^{2+}, and Na^{+} cations may be associated with the S and Cl volatiles. Furthermore, geochemical models of evaporation of sulfur-rich brines, derived from weathering of Martian basalt, indicate that the final liquid phase is concentrated in Fe^{3+}, Mg^{2+}, Na^{+}, Cl^{-}, and SO_4^{2-} (Chevrier and Altheide, 2008). Thus the solution compositions explored in this study are plausible for Martian surface and subsurface materials. The addition of bicarbonate to these initial mixtures served to investigate the potential interaction these highly acidic brines may have with native Martian carbonates, and the effect those carbonates would have on the resultant spectra.

For these initial experiments, samples were rapidly dehydrated at 21 °C in both vacuum and in 11% RH to force non-equilibrium precipitation conditions (Ling and Wang, 2010; Sklute et al., 2015; Wang et al., 2012; Xu et al., 2009; Xu and Parise, 2012). Though these low RH values are consistent with daytime RH values observed on the Martian surface (Harri et al., 2014; Savijarvi, 1995), and Martian surface temperatures can exceed 20 °C at the equator (Spanovich et al., 2006), this combination of RH-T values represents a narrow range of current Martian conditions. However, the goal of this study is to explore whether amorphous products can form from mixed component brines under rapid precipitation conditions, which could occur through multiple pathways (described above). The XRD characteristics, spectral properties, and preliminary observations of relative persistence under RH fluctuations of these newly considered mixed phases are presented."

3. Materials and methods

3.1. Brine dehydration experiments

The salt mixtures analyzed in this study are listed in Table 1. Each solution was made using ultrapure $Fe_2(SO_4)_3$ that had first been heated at 350 °C for 2 h to transform it from the bottled phase, which does not occur in nature, to the mineral mikasaite (Xu et al., 2009). Because Sklute et al. (2015) showed that amorphous phases formed through the deliquescence and dehydration of different starting materials show subtle spectral variations, the phase found in nature was considered the more appropriate starting material. Each salt was mixed with doubly de-ionized (DDI) water to create concentrated solutions: 0.10 M $Fe_2(SO4)_3$ (Alfa Aesar Puratronics, 99.998%), 1.00 M $CaCl_2 \cdot 2H_2O$ (VWR Amresco Life Science), 2.25 M $MgCl_2 \cdot 6H_2O$ (Acros Organics, 99+%), 0.348 M $FeCl_3 \cdot 6H_2O$ (VWR Amresco Life Science, 99+%), 0.596 M $NaHCO_3$ (BDH, 99.7+%), and 3.96 M NaCl (Fischer Scientific, 99+%). These solutions were then combined to create the molar ratio mixtures listed in Table 1. Initial 1:1 molar ratios were chosen for experimental simplicity with the exception of the $MgCl_2$-containing brines, where 2:1 ratios were also explored. Preliminary work (Rogers et al., 2016), which allowed each salt to deliquesce and then mixed them in volume ratios, produced similar results; variations between this and the preliminary work in Rogers et al., (2016) can be attributed to differing molar ratios.

Each mixed solution was split into two aliquots that were simultaneously dried at 21 °C in 1) 11% RH (LiCl buffered individual RH chambers, continually monitored by Lascar EL-USB-2-LCD Humidity Data Logger) to simulate evaporation on the Martian surface, and 2) under vacuum (Edwards E2M2 vacuum pump attached to an Applied Vacuum Engineering VF range bell jar) to simulate boiling on the Martian surface. The solutions were dried for 5 days under these conditions. Preliminary assessments of the relative stability of the amorphous solids were determined by monitoring the sample state during transfer from vacuum/low RH buffer to the VNIR/ATR spectrometers and XRD (Section 3.2) and later by

Table 1
Summary of salt mixtures used in these experiments.

Brine by moles	Figure abbreviation	Product[b] 11% RH	XRD[c]	Fig.	Product[b] vacuum	XRD[c]	Fig.
$CaCl_2$	$CaCl_2$	DNS	–	–	S; P	$CaCl_2 \cdot 4H_2O$	–
$MgCl_2$	$MgCl_2$	DNS	–	–	S; P	Bischofite	–
NaCl	NaCl	S; P	Halite	1(b)	S; P	Halite	–
$FeCl_3$	$FeCl_3$	DNS	–	–	S; P[a]	**Amorphous**	1(a)
$CaCl_2$–$Fe_2(SO_4)_3$	1CaCl:1FS	S; P	Gypsum + Amorphous	1(b)	S; P	Gypsum + Amorphous	1(b)
$2MgCl_2$–$Fe_2(SO_4)_3$	2MgCl:1FS	G	–	–	S; P	Cl_2 + Amorphous	1(b)
$MgCl_2$–$Fe_2(SO_4)_3$	1MgCl:1FS	S; P + G	**Amorphous**	1(a)	S; P + G	**Amorphous**	1(a)
NaCl–$Fe_2(SO_4)_3$	1NaCl:1FS	S; P	**Amorphous**	1(a)	S; P	**Amorphous**	1(a)
$FeCl_3$–$Fe_2(SO_4)_3$	1FeCl:1FS	G	–	–	S; P + G	**Amorphous**	1(a)
$CaCl_2$–$NaHCO_3$–$Fe_2(SO_4)_3$	1CaCl:1BC:1FS	S; P	Gypsum + Amorphous	1(b)	S; P	Gypsum + Amorphous	1(b)
$2MgCl_2$–$2NaHCO_3$–$Fe_2(SO_4)_3$	2MgCl:2BC:1FS	G	–	–	S; P	Halite + amorphous	1(b)
$MgCl_2$–$NaHCO_3$–$Fe_2(SO_4)_3$	1MgCl:1BC:1FS	S; P[a]	Halite + Amorphous	1(b)	S; P	Halite/Cl_2 + Amorphous	1(b)
NaCl–$NaHCO_3$–$Fe_2(SO_4)_3$	1NaCl:1BC:1FS	S; P	Halite + Amorphous	1(b)	S; P	Halite + Amorphous	1(b)
$FeCl_3$–$NaHCO_3$–$Fe_2(SO_4)_3$	1FeCl:1BC:1FS	G	–	–	S; P	**Amorphous**	1(a)
$Fe_2(SO_4)_3$–$NaHCO_3$	1FS:1BC	S; P	**Amorphous**	1(a)	S; P	**Amorphous**	1(a)
$Fe_2(SO_4)_3$	FS	S; P	**Amorphous**	1(a)	S; P	**Amorphous**	1(a)

[a] Sample was rapidly hydrating and was not solid by the end of the analysis.
[b] Physical nature of experimental product: S for solid, P for powder, G for gel, DNS for does not solidify.
[c] Crystalline phases are the best match from the Match2 database from a search allowing for all phases containing any of the listed cations; solid Cl_2 is unlikely in the sample.

monitoring the relative rate of deliquescence in individual MgCl-buffered (~33% RH) chambers for 56 days. However, back-buffering in these latter experiments may have substantially increased the RH range (~25–45%), and these results are, therefore, only used a broad guide to relative stability trends.

3.2. Sample characterization

Fresh samples of dried salts were ground under ambient RH conditions (20% RH) and then analyzed by VNIR spectroscopy or Fourier transform infrared (FTIR) MIR ATR spectroscopy. VNIR spectra were collected on powders loosely loaded into a matte black sample cup using an ASD FieldSpec 3Max VNIR spectrometer with a halogen light source (12.5 V, 4 A, 50 W, metal collimator) through a bare fiber. Incidence and emergence angles were fixed at 30° and 0° respectively. Spectra were calibrated to absolute reflectance through multiplying data with the reflectance spectrum of Spectralon acquired at Brown University RELAB. MIR ATR spectra were collected on a Thermo Fisher Nicolet 6700 FTIR equipped with a CsI beam splitter. Each spectrum was an average of 512 scans and background subtracted using Nicolet OMNIC software. ATR spectra provide IR absorbance data, which are not directly comparable to thermal emission spectra measured at Mars. ATR was used instead of thermal emission due to the relative speed of the measurement and the ability to measure the samples without heating or cooling. Though not directly comparable to Mars, the ATR data provide a useful measure of the degree of spectral changes between samples, and allow us to assess the composition of the product through comparison of the band positions with known molecular vibrational frequencies.

XRD patterns were obtained for each sample directly after each VNIR and MIR analysis to assess the crystallinity of the end products. XRD were obtained on a Rigaku MiniFlex (15 MA; 40 kV; 0.02°/step; 0.40 s/step) with a Cu Kα radiation source, optimized to reduce the fluorescence of iron-bearing samples, and using a quartz zero-background sample holder. Although the salt mixtures are only marginally stable under ambient RH conditions, previous work has shown that subsequent batches of the same compositions are spectroscopically consistent, allowing for fresh samples to be prepared directly prior to each analysis; each sample experienced ambient RH for less than 20 min, and XRD was the final analysis in each case (Sklute et al., 2015). Crystalline phases were identified using the Match2 database. All digital data are included as part of the supplemental material and posted on Dyar Lab website (Carey et al., 2017) as well as Stony Brook University Academic Commons (http://commons.library.stonybrook.edu/geo-articles/; search term "amorphous salts") for download and manipulation.

4. Results

Table 1 summarizes the experimental products of the brine dehydration experiments. XRD patterns for those products are shown in Fig. 1(a) (amorphous) and Fig. 1(b) (displaying some crystalline phases). Optical images of the dehydrated brines are shown in Fig. 2. The color of the resultant solids and powders changes markedly with composition. Fig. 3 shows the MIR ATR and VNIR reflectance spectra for all vacuum-dehydrated brine samples; spectra for brines dehydrated at low RH were spectrally similar, and are included in the supplementary material.

4.1. Brines with chlorides

Of the pure chloride solutions, only vacuum dehydrated $FeCl_3$ was amorphous and that sample was observed to rapidly hydrate into gel over the course of the analysis. It is included in Fig. 1(a) to show the difference between its diffuse scattering pattern (also known as the "amorphous hump") and those of the sulfates and mixed salts. The MIR ATR spectra for vacuum dehydrated $CaCl_2$, $MgCl_2$ and $FeCl_3$ are shown in Fig. 3(a). The most common feature in the MIR spectra for these hygroscopic salts is the ν_2 deformation mode of associated H_2O that occurs at ~1600 cm^{-1} (Guillermet and Novak, 1969). In $FeCl_3$, this appears as an asymmetric, broad absorption centered at 1589 cm^{-1}, whereas $MgCl_2$ and $CaCl_2$ have well defined doublets at 1652 cm^{-1}/1617 cm^{-1} for $MgCl_2$ and 1628 cm^{-1}/1612 cm^{-1} for $CaCl_2$.

VNIR spectra for these three salts, along with NaCl, are shown in Fig. 3(b). In this wavelength range, all features > ~1.3 μm are associated with overtones and combination modes of water and hydroxyl, along with vibrational features for carbonate and sulfate (Hunt and Salisbury, 1970). Most readily observable are the ~1.4 μm absorption due to the 2nd overtone of the asymmetric O–H stretch and the ~1.9 μm absorption due to the combination of the asymmetric O–H stretch with the H–O–H band. However, many other H_2O and OH combination bands can be found >1.8 μm (Hunt and Salisbury, 1970) and are expected in hydrated salts (Hanley et al., 2015). Because this wavelength range is very sensitive to hydration features, the NaCl sample is vacuum dehydrated for a more rigorous comparison to the other salts. The most prominent feature for NaCl and $CaCl_2$ are the asymmetric H_2O/OH

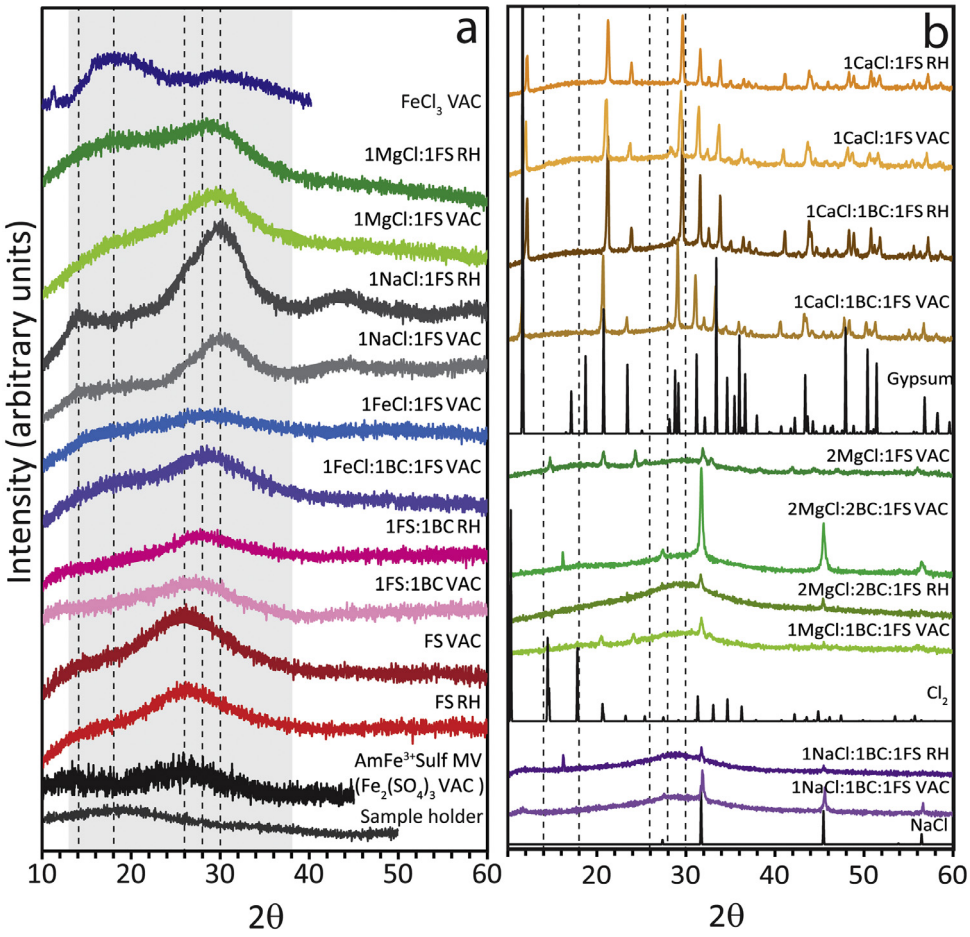

Fig. 1. (a) XRD data for the mixed salts that appear XRD-amorphous. The similar amorphous ferric sulfate (MV) from Sklute et al. (2015) is shown for reference. Although $FeCl_3$ VAC liquefied throughout the course of the measurement, it is included for comparison, as is the zero-background sample holder. Patterns are offset for clarity. The gray shaded region represents the range over which CheMin has detected XRD amorphous material: ~13–38° 2θ in Cu Kα (~15–45° 2θ for Co radiation; Bish et al., 2014; Bish et al., 2013). The CheMin Rocknest data show diffuse scattering with a single maximum at 30 ° 2θ (Co radiation; Rampe et al., 2016), which corresponds to ~26° 2θ in Cu Kα on this plot; (b) XRD data for mixed salts that show clear crystalline peaks with reference patterns for comparison. Note that only some of the constituents in the mixtures become crystalline phases and that crystalline pattern is superimposed on an amorphous diffuse scattering. Reference patterns are scaled and all patterns are offset for clarity. Dashed lines indicate the XRD maxima in the diffuse scattering for the various products.

combination bands at 1.935 μm and 1.959 μm (1.912 μm shoulder), respectively. $MgCl_2$ also shows this band at 1.972 μm, but also displays a number of other hydration features, including a doublet at 1.453 μm/~1.506 μm. $FeCl_3$ is almost entirely spectrally flat, and minimally reflective through this wavelength range.

4.1.1. $Fe_2(SO_4)_3$–$CaCl_2$

$Fe_2(SO_4)_3$–$CaCl_2$ mixtures solidified both under low RH and vacuum dehydration to solids that grind into ochre powders (Fig. 2); these powders do not form the glassy ambers that are the end product of many of the other dehydrated salt mixtures. The XRD patterns suggest the presence of gypsum (Fig. 1(b)), but with peaks slightly offset to larger 2θ values (smaller *d*-spacings) compared to gypsum samples in the Match2 database. Because both MIR and VNIR spectra of these mixtures show evidence for gypsum (see below), we attribute the slight offset in XRD peaks to small height errors due to the sample not fully filling the sample holder (this leads to systematic shifts in XRD reflections) or to possible compositional differences in the gypsum (due to substitution of other elements) resulting in peak shifts relative to pure gypsum. The gypsum signature is superimposed on diffuse scattering (Figs. 1 and 4). Fig. 4 compares the diffuse scattering in this sample to several of the amorphous products and shows that it best matches that for $FeCl_3$ VAC, suggesting that Ca is preferentially combined with SO_4 as the brine is dehydrated, and that the remaining Fe and Cl form an amorphous phase. However, where $FeCl_3$ alone was highly hygroscopic, the dehydrated $CaCl_2$–$Fe_2(SO_4)_3$ brine formed a relatively stable powder, demonstrating the extreme stability changes that can occur between amorphous phases from pure brines to those from a mixed brine.

The MIR spectra (Fig. 3(a)) for the $CaCl_2$-bearing mixtures show evidence for gypsum in the ν_4 sulfate absorptions (Lane, 2007) near 669 cm^{-1} and 598 cm^{-1} in $CaCl_2$–$Fe_2(SO_4)_3$ VAC. Although, where one of gypsum's main features is the SO_4 ν_3 absorption at ~1100 cm^{-1} (Lane, 2007), $CaCl_2$–$Fe_2(SO_4)_3$ VAC has a broadened feature centered at 1049 cm^{-1}. This shift to lower wavenumbers makes the absorption more consistent with that for pure amorphous ferric sulfate. The VNIR spectrum (Fig. 3(b)) displays a triplet at 1.447/1.487/1.533 μm that is reminiscent of the gypsum triplet at 1.452/1.490/1.535 μm. Additionally, the ferric iron in the sample is evident in the visible (VIS) wavelength range absorptions due to Fe^{3+} spin-forbidden crystal field transitions ($^6A_{1g}\rightarrow{}^4A_{1g}$, ^4E_g ~0.4 μm and $^6A_{1g}\rightarrow{}^4T_{1g}$ ~0.8 μm (Hunt and Salisbury, 1971)). In $CaCl_2$-bearing mixtures, these absorptions occur at 0.44 μm and 0.86 μm, respectively. Both of these absorptions are shifted to longer wavelengths than those for pure amorphous ferric sulfate (0.39 μm and 0.81 μm) or crystalline sulfates (e.g., 0.37 μm and 0.80 μm for rhomboclase).

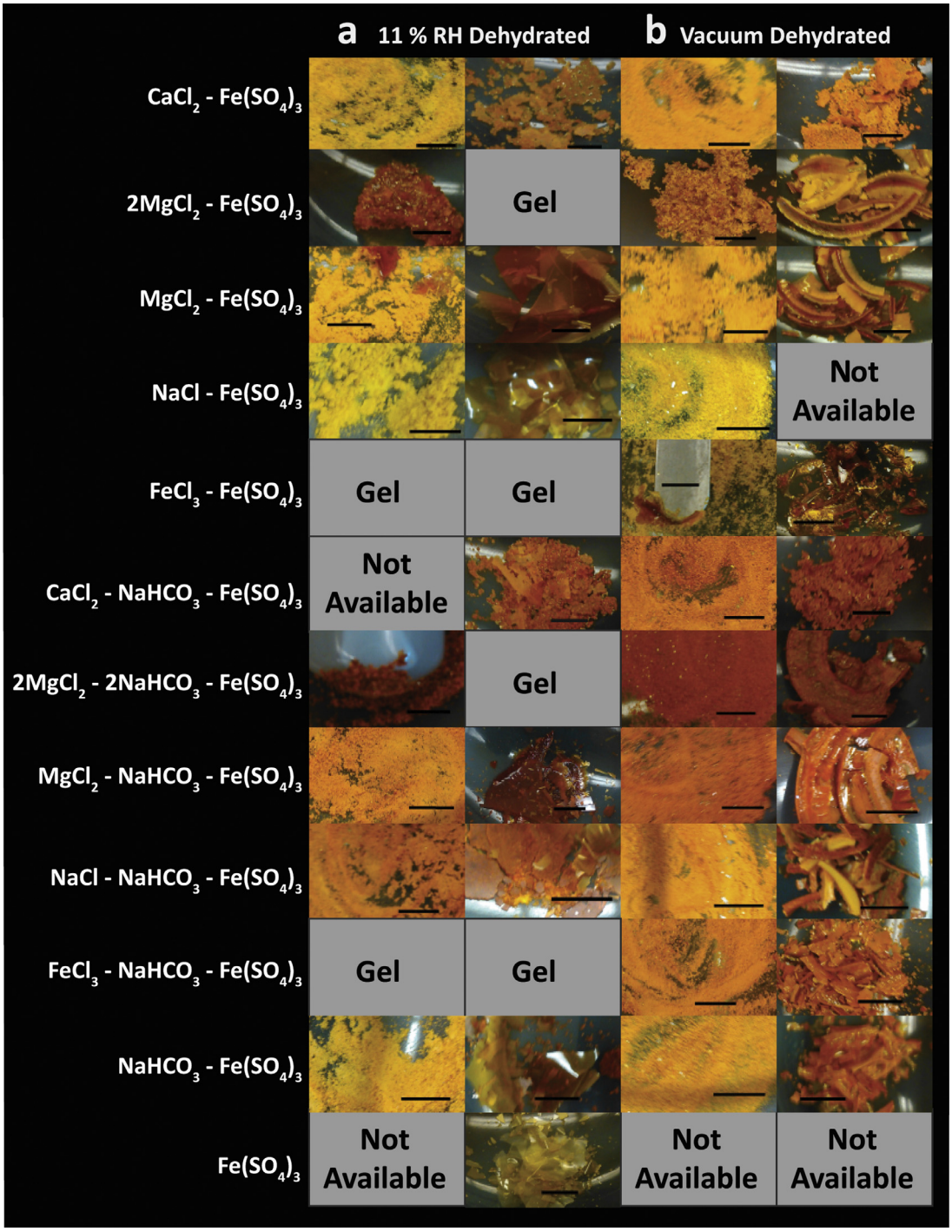

Fig. 2. Optical photographs of select solid and powdered mixed salts after 11% relative humidity (a) and vacuum (b) dehydration. Scale bar in all cases is 5 mm. The images in the right hand column of both (a) and (b) are the unaltered sample and the images in the left hand column of both (a) and (b) are the sample after it has been ground. Note the change in color with composition. Na-Bicarbonate appears to redden the samples.

4.1.2. $Fe_2(SO_4)_3$–$MgCl_2$

$Fe_2(SO_4)_3$–$MgCl_2$ mixtures partially solidified under both 11% RH and vacuum and when ground, produced ochre powders (Fig. 2) that are XRD amorphous for 1:1 molar ratios of $MgCl_2$:$Fe_2(SO_4)_3$. Increasing the molar ratio to $2MgCl_2$:$1Fe_2(SO_4)_3$ decreased the stability of the mixture against deliquescence, such that the 11% RH dehydrated sample did not fully solidify. Interestingly, the vacuum dehydrated sample did solidify and is crystalline with an XRD pattern that most closely matches the pattern for solid Cl_2 (Fig. 1(b)). While it is implausible that solid Cl_2 is present in the sample, halite and Cl_2 were the only reasonable matches when searching for all phases containing Fe, S, O, Mg, and Cl. It is possible, however, that the phase(s) resulting from this type of dehydration do not appear in the Match2 database. There is no indication in the XRD pattern of a sulfate-containing crystalline phase, but there is a diffuse scattering centered at ~30° 2θ (*d*-spacing ~3.0 Å) (versus 26° 2θ (*d*-spacing ~3.4 Å) for pure amorphous sulfates in this study).

In the MIR (Fig. 3(a)), $Fe_2(SO_4)_3$–$MgCl_2$ mixtures display sulfate and hydration features that most closely resemble those for the pure amorphous ferric sulfates, including the overlapping ν_1/ν_3 SO_4 absorptions (Lane, 2007) at ~912–1250 cm^{-1}, the ν_2 SO_4

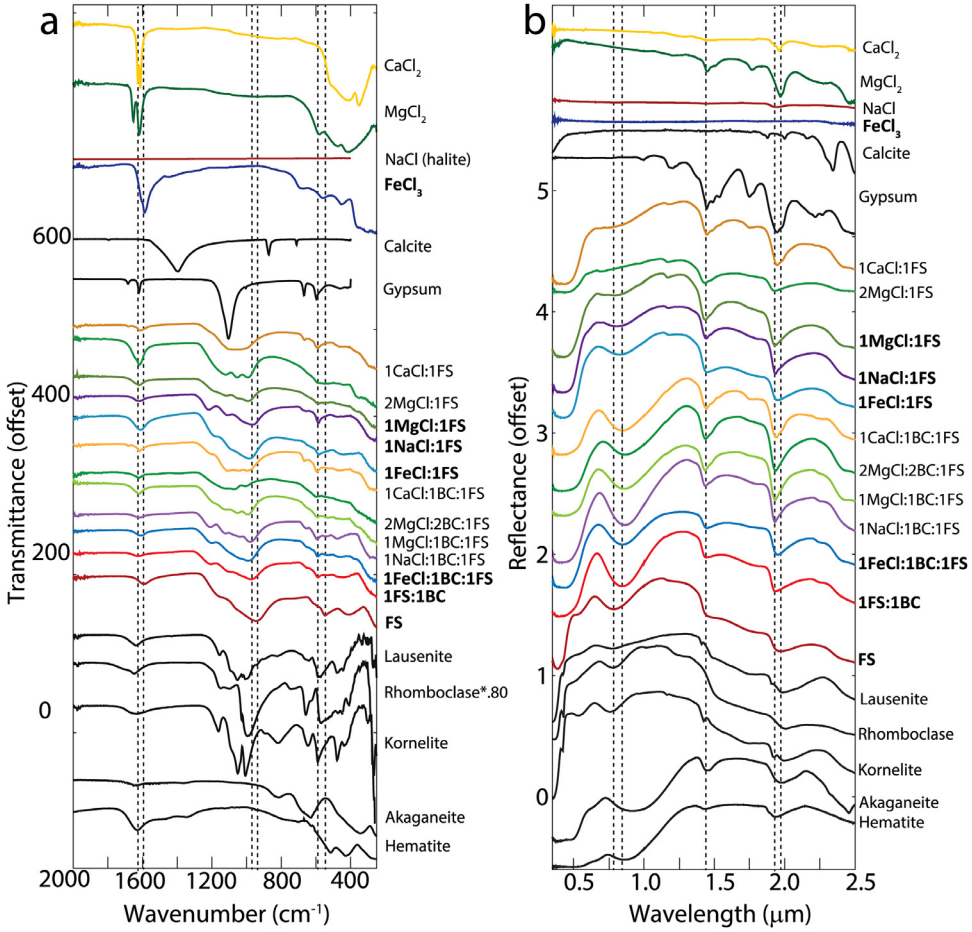

Fig. 3. FTIR ATR (a) and VNIR (b) spectra of vacuum dehydrated brines, along with several reference minerals. Bold sample names indicate XRD-amorphous materials with no crystalline phases detected. Mixtures are molar ratios and abbreviations are FS for $Fe_2(SO_4)_3$, MgCl for $MgCl_2$, FeCl for $FeCl_3$, CaCl for $CaCl_2$, and BC for $NaHCO_3$. The akaganéite and hematite are synthetic nanophase samples Ak102315 and Hem100915, respectively (Sklute et al., 2017); the rhomboclase is sample JB-JLB-74A aka MLS84; the kornelite is sample R16185 aka R16783; and the lausenite is sample 102,923. (a) Halite, gypsum, and calcite ATR spectra are from the RRUFF database (sample IDs R070292, R040029, and R040070, respectively (Lafuente et al., 2015; Dyar, 2015a)). All other ATR spectra were acquired at Stony Brook University. All spectra are offset for clarity. (b) Rhomboclase, kornelite, and lausenite VNIR spectra were taken from the RELAB database (Hiroi, 2000), and all other VNIR spectra were acquired at Stony Brook University. The gypsum sample is a pure crystal ground to < 125 μm. The halite sample is from Mount Holyoke College (Halite MHC1039 (Dyar, 2015b)). The rhomboclase, and kornelite VNIR spectra were collected by Janice Bishop with the NASA RELAB facility at Brown University, the kornelite VNIR spectrum was collected by Melissa Lane with the NASA RELAB facility at Brown University, and the rhomboclase, kornelite, and lausenite samples are further studied in Dyar et al. (2013). Spectra are offset for clarity. Dashed lines are included to guide the eye and correspond to the relative positions of absorption features for pure amorphous ferric sulfate (FS) and the ferric sulfate bicarbonate produce (1FS:1BC).

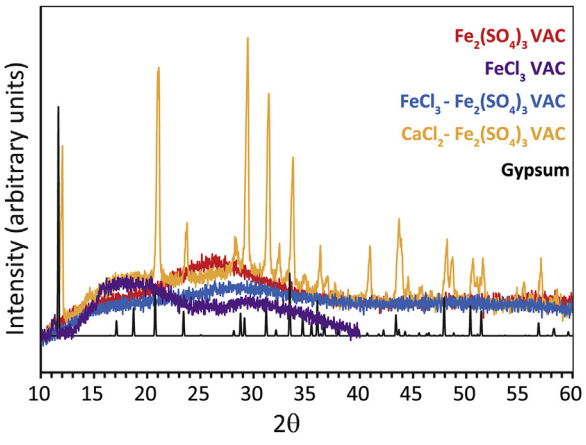

Fig. 4. XRD data for the vacuum dehydrated mixture of $CaCl_2$ and $Fe_2(SO_4)_3$ with that for three XRD amorphous samples displaying different types of diffuse scattering. The diffuse scattering under the gypsum peaks for this sample is most consistent with that for vacuum dehydrated $FeCl_3$. Patterns are offset to maximize overlap and reference pattern is offset and scaled for clarity.

absorption (Lane, 2007) at ~440 cm^{-1}, and the ν_4 SO_4 absorptions (Lane, 2007) from ~580–650 cm^{-1}. VNIR spectra (Fig. 3(b)) of 1:1 $MgCl_2$-bearing mixtures are similar to those for $CaCl_2$-bearing mixtures; they display deep, asymmetric hydration features at ~1.93 μm and ~1.43 μm (with a shoulder at ~1.48 μm). The ~1.93 μm absorption is significantly offset from that of $MgCl_2$ VAC (1.972 μm) as is the ~1.43/1.48 μm feature (compared to 1.45/1.51 μm). Like the $CaCl_2$-bearing samples, these spectra also possess absorptions in the VIS at ~0.43 μm ($^6A_{1g}\rightarrow{}^4A_{1g}$, ^4E_g) and ~0.85 μm ($^6A_{1g}\rightarrow{}^4T_{1g}$) consistent with Fe^{3+} spin forbidden crystal field transitions (Hunt and Salisbury, 1971), but also show a doublet ~0.69/0.72 μm for the $^6A_{1g}\rightarrow{}^4T_{2g}$ transition (Hunt and Salisbury, 1971). The 2:1 $MgCl_2$:$Fe_2(SO_4)_3$ sample, which was not stable enough for MIR analysis, shows much less spectral contrast in the VNIR and the position of the Fe^{3+} features are shifted to ~0.45 μm, ~0.70/0.72 μm, and ~0.78 μm. In addition, a new doublet is visible at ~0.63/0.65 μm. While the $^6A_{1g}\rightarrow{}^4A_{1g}$, ^4E_g for these samples is still shifted to longer wavelengths than that for pure amorphous or crystalline sulfates, the $^6A_{1g}\rightarrow{}^4T_{1g}$ in the 2:1 mixture is more consistent with these reference phases.

4.1.3. $Fe_2(SO_4)_3$–NaCl

$Fe_2(SO_4)_3$–NaCl mixtures solidified under both 11% RH and vacuum to form solids that grind into yellow-ochre powders (Fig. 2). These powders are XRD amorphous with a bimodal diffuse scattering pattern peaking at ~14° 2θ (*d*-spacing ~6.3 Å) and ~30° 2θ (*d*-spacing ~3.0 Å). In the MIR (Fig. 3(a)), these dehydrated brines are spectrally similar to pure amorphous ferric sulfate in the appearance of their SO_4 ν_1/ν_3 absorption band envelopes, although the minimum at 966 cm^{-1} is shifted to lower wavenumbers than that of pure amorphous ferric sulfate (980 cm^{-1}). The ν_4 SO_4 is also shifted slightly but to higher wavenumbers (586 cm^{-1} compared to 582 cm^{-1}). In the NIR (Fig. 3(b)), depth and position of the hydration features are closer to the other chloride-bearing mixtures, shifted to shorter wavelengths than pure amorphous ferric sulfate. In the VIS, the position of the Fe^{3+} spin-forbidden crystal field transitions are shifted to higher wavelengths (~0.41 μm vs. 0.39 μm for $^6A_{1g}\rightarrow{}^4A_{1g}$, ^4E_g; ~0.87 μm vs. ~0.81 μm for $^6A_{1g}\rightarrow{}^4T_{1g}$) compared to pure, amorphous ferric sulfate. There also appears to be a flattening to the top of the VIS maximum, which may indicate an unresolved feature.

4.1.4. $Fe_2(SO_4)_3$–$FeCl_3$

$Fe_2(SO_4)_3$–$FeCl_3$ mixtures did not solidify under 11% RH. However, those dehydrated by vacuum partially solidified into amber solids that grind into ochre powders (Fig. 2) that are XRD amorphous (Fig. 1(a)) with almost no diffuse scattering (however the sample was slightly tacky after analysis). Previous volume ratio experiments revealed that increasing the relative amount of sulfate with respect to chloride increased the stability of the mixture against deliquescence. In the MIR, the $Fe_2(SO_4)_3$–$FeCl_3$ mixture is almost identical to pure, amorphous ferric sulfate below ~1200 cm^{-1} in both band position and overall appearance of band envelopes although the SO_4 ν_4 absorption is slightly shifted as it was in the NaCl-bearing mixture. The two spectra, however, vary in the position of the H_2O deformation mode (Guillermet and Novak, 1969) which is 20 cm^{-1} lower (1610 cm^{-1}) in the $FeCl_3$-bearing sample. This similarity does not hold in the VNIR. Here (Fig. 3(b)), the $Fe_2(SO_4)_3$–$FeCl_3$ sample displays absorption positions that are much closer to those in the other chloride-bearing mixtures in both the position and appearance of the hydration features ~1.4 μm and 1.9 μm and the position and appearance of the spin-forbidden crystal field transitions at 0.44 μm and 0.85 μm for this sample compared to 0.39 μm, 0.55 μm, and 0.81 μm for pure amorphous ferric sulfate.

4.2. Brines with $NaHCO_3$

The addition of bicarbonate solutions to chloride- and sulfate-bearing brines caused the solution to bubble rapidly, likely due to the rapid release of CO_2 gas from the concentrated brine. During this process, the pH of the solution increases appreciably. Upon deliquescence, a saturated solution of $Fe_2(SO_4)_3$ has a pH of 0.78. When an equal volume of saturated $NaHCO_3$ solution was added, after all bubbling had ceased, the pH increased to 2.48. Thus, the addition of $NaHCO_3$ resulted in the introduction of sodium and hydroxl to the solution, leading to a partial neutralization, but it is unlikely that carbonate was added (see discussion of spectral features below). Interestingly, all solutions to which $NaHCO_3$ was added were more stable against deliquescence than their $NaHCO_3$-free counterparts, suggesting that Na and/or OH play a role in the stabilization of the amorphous phase. While the exact mechanism of stabilization is unclear at this time, it is likely that the partially neutralized, bicarbonate-bearing solutions have fewer available charged or polar groups to which atmospheric water can bond. Because the bulk phase and surface structure are still unknown for most of these compounds, further speculation on the stabilization mechanism is unwarranted at this time.

In addition to increased stability/decreased hygroscopicity, the powders created from the $NaHCO_3$-bearing solutions were visibly redder than those without $NaHCO_3$ (Fig. 2). This can be seen spectrally in the ubiquitously altered appearance of the VIS absorptions (Fig. 3). Because the exact phase(s) and surface structures of these solids are still unknown, we cannot speculate as to the mechanism, but clearly the crystal field splitting energy of the iron in the samples is being altered by the presence of Na^+ or the decreased pH of the solution from which they precipitate.

If carbonate or bicarbonate were present in the end phase, some spectral features near the location of the CO_3 fundamental vibrations (~840–900 cm^{-1}, ~670–770 cm^{-1}, and ~1385–1493 cm^{-1}, Huang and Kerr, 1960) would be expected. Bicarbonate minerals have slightly shifted bands (~1409–1316 cm^{-1}, ~1047 cm^{-1}, ~1035 cm^{-1}, ~837 cm^{-1}, and ~694 cm^{-1}, Huang and Kerr, 1960) that can be used to distinguish them from carbonates (Joshi et al., 2013). In the VNIR, carbonates exhibit several CO_2 bend and stretch overtone and combination bands (Gaffey, 1987), of which the band at ~2.3 μm is usually the most prominent, with bands at ~1.88 μm, ~2.00 μm, and ~2.16 μm being observable in very carbonate rich samples (Cloutis et al., 2010). In bicarbonate minerals, these bands are slightly shifted. For instance, trona shows peaks at 1.5 μm, 1.74 μm, 1.94 μm, 2.03 μm, and 2.22 μm (Kodikara et al., 2012).

4.2.1. $Fe_2(SO_4)_3$–$NaHCO_3$

$Fe_2(SO_4)_3$–$NaHCO_3$ dehydrated brines are XRD amorphous (Fig. 1(a)) with a diffuse scattering centered ~28° 2θ (*d*-spacing ~3.2 Å), shifted from that of pure, amorphous ferric sulfates, which showed this feature at ~26° 2θ (*d*-spacing ~3.4 Å). The MIR spectra (Fig. 3(a)) of bicarbonate-bearing samples are quite similar to those for bicarbonate-free samples, but there is a slight increase in fine structure in the SO_4 band envelopes. The greatest spectral difference resulting from bicarbonate addition is significant changes to the VIS structure that is common to all bicarbonate-bearing mixtures (Fig. 3(b)). There is almost a complete loss of the Fe^{3+} $^6A_{1g}\rightarrow{}^4T_{2g}$ (~0.55 μm) transition and the $^6A_{1g}\rightarrow{}^4T_{1g}$ (~0.86 μm) absorption becomes much more defined. In addition, this feature is shifted from that of the pure ferric sulfates (~0.81 μm), making it closer to that expected for nanophase hematite. These changes lead to an apparent narrowing of the VIS maximum from ~0.49–0.66 μm in pure amorphous ferric sulfate or ~0.57–0.72 μm in chloride-bearing, bicarbonate-free samples to a narrow maximum ~0.68 μm in bicarbonate-bearing samples. These changes also lead to an apparent narrowing of the near-infrared (NIR) maxima that occurs at ~1.1–1.4 μm in pure amorphous ferric sulfate but 1.2–1.4 μm in $Fe_2(SO_4)_3$–$NaHCO_3$ mixtures and only ~1.3–1.4 μm in $Fe_2(SO_4)_3$–$NaHCO_3$–chloride bearing mixtures. Another change seen is the appearance of an absorption at ~2.24 μm that is not present in bicarbonate-free samples. Although this could indicate the presence of bicarbonate, which has a feature at ~2.2 μm, there is no evidence for carbonate/bicarbonate in the MIR data. Rather, the ~2.24 μm feature is likely caused by an O–H or metal-OH stretching overtone.

4.2.2. $Fe_2(SO_4)_3$–$NaHCO_3$–$CaCl_2$

$Fe_2(SO_4)_3$–$NaHCO_3$–$CaCl_2$ brines dehydrated into stable red-ochre powders (Fig. 2) that are XRD matches for gypsum overlaid on the same diffuse scattering pattern as the bicarbonate free samples (Fig. 1(b)). However, their primary features in MIR spectra bear little resemblance to that of gypsum (Fig. 3(a)). They instead appear much like that for amorphous ferric sulfate, although with shifted band positions. Like the bicarbonate-free brines, NIR spectra (Fig. 3(b)) for these samples more closely resemble that for

gypsum with a triplet ~1.44/1.49/1.53 μm along with other common hydration and sulfate features. Carbonate/bicarbonate features are not apparent in either data set for these samples.

4.2.3. $Fe_2(SO_4)_3$–$NaHCO_3$–$MgCl_2$

$Fe_2(SO_4)_3$–$NaHCO_3$–$MgCl_2$ brines partially solidified under low RH and fully solidified under vacuum into red-ochre solids that grind into powders, where $2MgCl_2$–$2NaHCO_3$–$Fe_2(SO_4)_3$ is much redder than $MgCl_2$–$NaHCO_3$–$Fe_2(SO_4)_3$ (Fig. 2). None of these mixtures are XRD amorphous. Like the bicarbonate-free samples, they show XRD reflections of halite and/or Cl_2, and the pattern is overlaid on diffuse scattering (Fig. 1(b)). In the MIR (Fig. 3(a)), these bicarbonate-bearing mixtures display sulfate and hydration features similar to those for bicarbonate-free samples, with the SO_4 ν_1/ν_3 band envelope differing between the 1:1 and 2:1 $MgCl_2$:$Fe_2(SO_4)_3$ samples. However, in the 2:1 samples, the H_2O ν_2 deformation mode (Guillermet and Novak, 1969) ~1620 cm^{-1} is no longer significantly deeper than that for the 1:1 samples, as was the case for the bicarbonate-free series (Fig. 3(a)). Again, there is no sign of carbonate or bicarbonate in the spectra for these samples.

4.2.4. $Fe_2(SO_4)_3$–$NaHCO_3$–$NaCl$

$Fe_2(SO_4)_3$–$NaHCO_3$–NaCl brines solidified under both 11% RH and vacuum into solids that grind into orange-ochre powders (Fig. 2), showing the reddening effect of the sodium bicarbonate. These samples show XRD structure that matches halite superimposed on diffuse scattering lacking the second low 2θ maximum seen in the bicarbonate-free samples (Fig. 1b). In the MIR (Fig. 3(a)), these samples have the same basic shape as the pure, amorphous ferric sulfates but show more fine structure. In the VNIR (Fig. 3(b)), $Fe_2(SO_4)_3$–$NaHCO_3$–NaCl are spectrally similar to the other bicarbonate- and chloride- containing dehydrated brines. Here again, an absorption at ~2.25 μm is present in bicarbonate-bearing samples that is not seen in bicarbonate free samples.

4.2.5. $Fe_2(SO_4)_3$–$NaHCO_3$–$FeCl_3$

$Fe_2(SO_4)_3$–$NaHCO_3$–$FeCl_3$ brines did not solidify under 11% RH but do solidify under vacuum into XRD amorphous (Fig. 1(a)) solids that grind into orange-ochre powders (Fig. 2). The diffuse scattering for this sample peaks ~28° 2θ (*d*-spacing ~3.2 Å), in between that for pure amorphous ferric sulfate (26° 2θ) and that for the other chloride-containing samples (~30° 2θ). Like the bicarbonate-free sample, the MIR spectrum (Fig. 3(a)) for this dehydrated brine is similar to that of pure, amorphous ferric sulfate with the exception of the H_2O ν_2 deformation mode, which is noticeably shifted to shorter wavenumbers. Interestingly, one of the products of preliminary long-term stability experiments for this mixture was jarosite.

5. Discussion

Of the samples investigated, $Fe_2(SO_4)_3$ mixed with NaCl, $FeCl_3$, $NaHCO_3$, $MgCl_2$, and $FeCl_3 + NaHCO_3$ can all form purely XRD amorphous products. The remaining mixtures exhibit XRD patterns that contain sharp peaks and diffuse scattering, indicating the presence of both crystalline and amorphous phases. Furthermore, the crystalline phase(s) represented by the sharp peaks cannot account for the elemental composition of the mixtures by themselves. Therefore, all mixtures result in some amount of XRD amorphous components. For mixtures that allowed for the combination of Ca and SO_4, the diffuse scattering indicative of the amorphous phase in the mixture was somewhat obscured by the intense gypsum XRD reflections (e.g., Figs. 1(b) and 4). In contrast, gypsum-related features were weak in the MIR, with the amorphous component being dominant.

For pure chlorides, only $FeCl_3$ became XRD amorphous. These Fe(III)–chloride brine dehydration products, as well as the vacuum-dehydrated Ca and Na–chloride brines, exhibit weak-to-absent hydration features that could be difficult to detect from orbital observations. In the mixture with $2MgCl_2$:$1Fe_2(SO_4)_3$, hydration features due to sulfate were greatly weakened; higher chloride to sulfate ratios could result in complete masking of these features. These observations raise the possibility that Martian chloride-bearing units (e.g., Osterloo et al., 2008) may not necessarily be composed of NaCl (inferred in previous studies based on weak-to-absent hydration features in the orbital NIR data (Jensen and Glotch, 2011)). Rather, desiccated $FeCl_3$ $MgCl_2$, or $CaCl_2$ could contribute to these deposits. Furthermore, because increasing the chloride to sulfate ratio significantly decreases the intensity of the sulfate-related features in the MIR, hydration features in the NIR, and Fe^{3+} crystal field splitting features in the VIS, it is possible that other components (such as sulfate) could be obscured if present in low abundance in an amorphous multicomponent salt.

Spectrally, most of the multicomponent amorphous salts appeared similar to amorphous ferric sulfate in the MIR. In the NIR, multicomponent amorphous salts exhibit slightly broadened hydration features and would likely be difficult to distinguish from pure polyhydrated crystalline sulfates. Determining the chemistry of the amorphous salts from spectra alone would be further complicated when mixed with other materials (e.g., silicates). Nevertheless, the important point is that amorphous salt phases can be comprised of multiple components across many concentrations.

Deliquescence of ferric sulfates is key to the formation of near-surface amorphous ferric sulfate-containing salts, under present-day conditions. The RH value necessary for ferric sulfate deliquescence (> ~75%) has thus far only been determined for a temperature of 25 °C (Xu et al., 2009). To date, no experimental data exist for the deliquescence RH (DRH) of crystalline ferric sulfate below 25 °C, but because DRH studies for other highly deliquescent salts like chlorides and perchlorates show increased DRH values at lower temperatures (Gough et al., 2011; Nuding et al., 2014; Gough et al., 2016), the DRH for ferric sulfate is likely to be higher than 75% RH for typical Martian surface temperatures (e.g., <0 °C). Because RH is highest during the coldest parts of the diurnal cycle (e.g., Savijarvi, 1995), RH-T conditions at the surface may not be conducive to deliquescence of crystalline ferric sulfate. However, in the shallow subsurface, crystalline sulfates with higher hydration states could act as humidity buffers within the soils, maintaining high RH levels in the near subsurface, even at moderate temperatures. For example, a closed container of ferricopiapite maintained a headspace RH level of ~75% at −10 °C, and epsomite maintained RH of ~96% (Wang et al., 2013). These RH levels and temperature conditions meet the experimental RH-T conditions needed to deliquesce the less-hydrated ferric sulfates such as rhomboclase and ferric sulfate pentahydrate (Lu and Wang, 2013). In other words, deliquescence of less hydrated ferric sulfates could potentially occur in the near-subsurface if other salts with higher hydration states were present. Alternatively, if the RH was not high enough for ferric sulfate to deliquesce, but high enough for more deliquescent salts such as ferric chloride to deliquesce, ferric sulfate could potentially dissolve upon coming into contact with that ferric chloride brine. This would produce highly concentrated acidic brines that could dissolve neighboring phases, including carbonates and clay minerals, and re-precipitate mixed-component amorphous salts. Areas exposed to repeated deliquescence cycles could result in further dissolution and/or incorporation of silicate grains into salt glasses, resulting in indurated surfaces. These transient acids could actively prevent carbonate minerals from existing at the Martian surface or near subsurface. Further work is needed to understand the deliquescence behavior of mixed salt grains un-

der Martian conditions (e.g., Gough et al., 2014), as well as the effect of neighboring silicate grains on this process.

Though not an in-depth study of stability, the results of our 1:1 and 2:1 $Fe_2(SO_4)_3$:$MgCl_2$ experiments and previously examined volume ratio experiments do suggest that the stability of amorphous phases against deliquescence is dependent upon the element proportions in the original mixture. Therefore, depending on composition, salt mixtures could be variably stable or deliquescent under Martian surface and subsurface conditions. If amorphous salts are present on Mars, they could play a role in present day deliquescence-related phenomena such as recurring slope lineae (e.g., McEwen et al., 2011; Ojha et al., 2015; Heinz et al., 2016) or soil induration (e.g., Bishop et al., 2002), as many of these salts were found to be more deliquescent than their crystalline counterparts. For example, at 25 °C, amorphous ferric sulfate deliquesced at 33% RH within a few hours (Gregerson et al., 2017), compared to a DRH of 75% for the crystalline ferric sulfate phase at this temperature (Xu et al., 2009). Further work is needed to determine the end products of long-term RH cycling for pure and mixed brines.

6. Conclusions

Our experiments showed that $FeCl_3$, $Fe_2(SO_4)_3$, $Fe_2(SO_4)_3 + NaHCO_3$, $NaCl + Fe_2(SO_4)_3$, $MgCl_2 + Fe_2(SO_4)_3$, and $FeCl_3 + Fe_2(SO_4)_3 + NaHCO_3$ brines all solidify either by 11% RH, vacuum, or both into XRD amorphous solids that grind easily into powders under low RH (< 20%). The remaining $Fe_2(SO_4)_3$-containing samples all solidify by either 11% RH, vacuum, or both into a mixture of crystalline and amorphous phases. Dehydration of pure $CaCl_2$, $MgCl_2$, and NaCl brines results in only crystalline products. The amorphous products exhibit measurable differences in the shape and center position of the XRD diffuse scattering that can be compared with data from Mars Science Laboratory; the 2θ values are within the range of the amorphous component measured for Rocknest soils by CheMin. Spectrally, multicomponent amorphous ferric sulfate-bearing salts appear broadly similar to pure amorphous ferric sulfate in the MIR. In the NIR, the addition of chloride results in the sharpening of the ~1.4 μm and ~1.9 μm absorptions along with a shift in the position of the ~1.9 μm absorption to shorter wavelengths. In the VIS the addition of chloride and/or bicarbonate shifts the position and depth of the Fe^{3+} spin forbidden crystal field transition absorptions. The differences between the MIR and VNIR evidence for additional phases in these ferric sulfate-bearing mixtures is likely due to the relative prominence of the absorptions of specific groups in each of these wavelength ranges, the bonding environment for each group, and relative sensitivity of the type of spectroscopy to the bonding environment. In the MIR, where sulfate absorptions are prominent, the compositional differences between these phases results in minimal spectral changes, suggesting that either the energetic environment around the sulfate groups is similar between compositions, or the next nearest neighbor to the S atom in these compounds has an unresolvable effect on the sulfur-oxygen bond energy. Broadening of the sulfate features in this wavelength range due to the amorphous or fine-grained nature of the materials may contribute to this loss of resolution. In the NIR, the energy of the water and hydroxyl bonds are more effected by the differing compositional environments, but here, the presence or absence of chloride seems to be the dominant factor, with only minor gradations between chloride species. In the VIS, however, the direct bonding environment of the ferric iron must be more significantly impacted by the changes in composition, thus causing a larger variation in the position of the Fe^{3+} spin-forbidden crystal field transition absorptions.

While more work is needed to identify and characterize the phase(s) present in these amorphous or mixed crystalline-amorphous solids as well as to determine their stability under Mars-relevant conditions, it is clear from this work that the composition and relative abundance of cations in the original brine result in differences in the phase(s), spectra, and stability of the products. These findings open up the possibility that XRD amorphous phases could precipitate from saturated mixed brines on the Maritan surface. The amorphous material will depend on the composition of the original brine and may consist of a single amorphous phase within a solid solution or a mixture of compositionally distinct amorphous phases. Because amorphous sulfates deliquesce at lower RH values than crystalline sulfates, if present in Martian soils, they might serve as agents of water vapor exchange between regolith and atmosphere in the past or present day.

One important implication of this work is that phase transformations may occur in returned Martian samples. If collected Martian surface material contains deliquescent amorphous phases, those samples may become altered while cached or during their return to Earth. This could be especially perplexing if minerals originally present in the sample were dissolved as a result of coming into contact with a deliquesced acidic salt. Understanding the composition and stability of these potential amorphous phases could be crucial to preservation and interpretation of returned samples.

Acknowledgments

Elizabeth Sklute acknowledges support from NASA through the RIS^{4}E SSERVI at Stony Brook University. Deanne Rogers and Jason Gregerson acknowledge support from the NASA Planetary Geology and Geophysics program (NNX12AO45G). We thank Ralph Milliken for the Spectralon spectrum. We thank Liz Rampe and reviewer 2 for their insightful comments and suggestions.

References

Bish, D., et al., 2014. The first X-ray diffraction measurements on Mars. IUCrJ 1, 514–522. doi:10.1107/S2052252514021150.

Bish, D.L., et al., 2013. X-ray diffraction results from Mars Science Laboratory: mineralogy of Rocknest at Gale Crater. Science 341. 1238932–1238932 doi: 10.1126/science.1238932.

Blake, D., et al., 2012. Characterization and calibration of the CheMin mineralogical instrument on Mars Science Laboratory. Space Sci. Rev. 170, 341–399. doi:10.1007/s11214-012-9905-1.

Bishop, J.L., Murchie, S.L., Pieters, C.M., Zent, A.P., 2002. A model for formation of dust, soil, and rock coatings on Mars: physical and chemical processes on the Martian surface. J. Geophys. Res. Planets 107, E11. doi:10.1029/2001JE001581.

Blake, D.F., et al., 2013. Curiosity at Gale Crater, Mars: characterization and analysis of the Rocknest sand shadow. Science 341. 1239505–1239505 doi: 10.1126/science.1239505.

Carey, C., Dyar, M.D., Boucher, T., Giguere, S., 2017. Web-based software for preprocessing, matching, fitting, prediction, and visualization of spectroscopic data: the data exploration, visualization, and analysis of spectra (DEVAS) website. Presented at the 48th Lunar and Planetary Science Conference Abstract #1097.

Chevrier, V.F., Altheide, T.S., 2008. Low temperature aqueous ferric sulfate solutions on the surface of Mars. Geophys. Res. Lett. 35, L22101. doi:10.1029/2008GL035489.

Chipera, S.J., Vaniman, D.T., 2007. Experimental stability of magnesium sulfate hydrates that may be present on Mars. Geochim. Cosmochim. Acta. 71, 241–250. doi:10.1016/j.gca.2006.07.044.

Cloutis, E.A., Grasby, S.E., Last, W.M., Léveillé, R., Osinski, G.R., Sherriff, B.L., 2010. Spectral reflectance properties of carbonates from terrestrial analogue environments: implications for Mars. Planet. Space Sci. 58, 522–537. doi:10.1016/j.pss.2009.09.002.

Dehouck, E., Gaudin, A., Chevrier, V., Mangold, N., 2016. Mineralogical record of the redox conditions on early Mars. Icarus 271, 67–75. doi:10.1016/j.icarus.2016.01.030.

Dehouck, E., McLennan, S.M., Meslin, P.-Y., Cousin, A., 2014. Constraints on abundance, composition, and nature of X-ray amorphous components of soils and rocks at Gale crater, Mars. J. Geophys. Res. Planets. 119, 2640–2657. doi:10.1002/2014JE004716.

Dehouck, E., McLennan, S.M., Meslin, P.-Y., Cousin, A., Science Team, MSL, 2015. The X-ray amorphous components of the Rocknest soil and Sheepbed mudstone (Gale Crater, Mars): minimum abundance, compositional ranges and possible constituents. Presented at the 46th Lunar and Planetary Science Conference Abstract #1946.

Dyar, M.D., Breves, E., Jawin, E., Marchand, G., Nelms, M., O'Connor, V., Peel, S., Rothstein, Y., Sklute, E.C., Lane, M.D., Bishop, J.L., Mertzman, S.A., 2013. Mössbauer parameters of iron in sulfate minerals. Am. Mineral. 98, 1943–1965. doi:10.2138/am.2013.4604.

Dyar, M.D., 2015a. RRUFF FTIR Dataset Project Superman. http://nemo.cs.umass.edu:54321/explorer?ds_kind=FTIR&ds_name=RRUFFAccessed 21 April 2017.

Dyar, M.D., 2015b. Watts minerals FTIR dataset Project Superman. http://nemo.cs.umass.edu:54321/explorer?ds_kind=FTIR&ds_name=Watts%20Minerals. Accessed 8 July 2015.

Franks, F., 1993. Solid aqueous-solutions. Pure Appl. Chem. 65, 2527–2537. doi:10.1351/pac199365122527.

Gaffey, S., 1987. Spectral reflectance of carbonate minerals in the visible and near-infrared (0.35-2.55 μm) – anhydrous carbonate minerals. J. Geophys. Res. Solid Earth Planets. 92, 1429–1440. doi:10.1029/JB092iB02p01429.

Golden, D.C., Ming, D.W., Schwandt, C.S., Morris, R.V., Yang, S.V., Lofgren, G.E., 2000. An experimental study on kinetically-driven precipitation of calcium-magnesium-iron carbonates from solution: implications for the low-temperature formation of carbonates in martian meteorite Allan Hills 84001. Meteorit. Planet Sci. 35, 457–465.

Gough, R.V., Chevrier, V.F., Baustian, K.J., Wise, M.E., Tolbert, M.A., 2011. Laboratory studies of perchlorate phase transitions: support for metastable aqueous perchlorate solutions on Mars. Earth Planet Sci. Lett. 312, 371–377. doi:10.1016/j.epsl.2011.10.026.

Gough, R.V., Chevrier, V.F., Tolbert, M.A., 2016. Formation of liquid water at low temperatures via the deliquescence of calcium chloride: implications for Antarctica and Mars. Planet Space Sci. 131, 79–87. doi:10.1016/j.pss.2016.07.006.

Gough, R.V., Chevrier, V.F., Tolbert, M.A., 2014. Formation of aqueous solutions on Mars via deliquescence of chloride-perchlorate binary mixtures. Earth Planet Sci. Lett. 393, 73–82. doi:10.1016/j.epsl.2014.02.002.

Gregerson, J., Rogers, A.D., Sklute, E.C., Reeder, R.J., Dyar, M.D., 2017. Phase transitions of amorphous iron(III) sulfates at an intermediate humidity. Presented at the 48th Lunar and Planetary Science Conference Abstract #2100.

Guillermet, J., Novak, A., 1969. Infrared spectra of hydrated magnesium chlorides and bromides. J. Chim. Phys. Phys. Chim. Biol. 66, 68–80.

Hanley, J., Chevrier, V.F., Barrows, R.S., Swaffer, C., Altheide, T.S., 2015. Near- and mid-infrared reflectance spectra of hydrated oxychlorine salts with implications for Mars: spectra of perchlorates. J. Geophys. Res. Planets. 120, 1415–1426. doi:10.1002/2013JE004575.

Harri, A., Genzer, M., Kemppinen, O., Haberle, R., Polkko, J., Savijärvi, H., 2014. Mars Science Laboratory relative humidity observations: initial results. J. Geophys. Res. Planets. 119, 2132–2147. doi:10.1002/2013JE004514.

Heinz, J., Schulze-Makuch, D., Kounaves, S.P., 2016. Deliquescence-induced wetting and RSL-like darkening of a Mars analogue soil containing various perchlorate and chloride salts. Geophys. Res. Lett. 43, 4880–4884. doi:10.1002/2016GL068919.

Huang, C.K., Kerr, P.F., 1960. Infrared study of the carbonate minerals. Am. Mineral. 45, 311–324.

Hunt, G.R., Salisbury, J.W., 1970. Visible and near-infrared spectra of minerals and rocks; I, Silicate minerals. Mod. Geol. 1, 283–300.

Hunt, G.R., Salisbury, J.W., 1971. Visible and near-infrared spectra of minerals and rocks: II. Carbonates. Mod. Geol. 2, 23–30.

Jensen, H.B., Glotch, T.D., 2011. Investigation of the near-infrared spectral character of putative martian chloride deposits. J. Geophys. Res. Planets 116, E00J03. doi:10.1029/2011JE003887.

Joshi, S., Kalyanasundaram, S., Balasubramanian, V., 2013. Quantitative analysis of sodium carbonate and sodium bicarbonate in solid mixtures using Fourier transform infrared spectroscopy (FT-IR). Appl. Spectrosc. 67, 841–845.

Kodikara, G.R.L., Woldai, T., van Ruitenbeek, F.J.A., Kuria, Z., van der Meer, F., Shepherd, K.D., van Hummel, G.J., 2012. Hyperspectral remote sensing of evaporate minerals and associated sediments in Lake Magadi area, Kenya. Int. J. Appl. Earth Obs. 14, 22–32. doi:10.1016/j.jag.2011.08.009.

Lafuente, B., Downs, R.T., Yang, H., Stone, N., 2015. The power of databases: the RRUFF project. In: Armbruster, T., Danisi, R.M., De Gruyter, W. (Eds.), Highlights in Mineralogical Crystallography, pp. 1–30. http://rruff.info/about/downloads/HMC1-30.pdf.

Lane, M.D., 2007. Mid-infrared emission spectroscopy of sulfate and sulfate-bearing minerals. Am. Mineral. 92, 1–18. doi:10.2138/am.2007.2170.

Leshin, L.A., et al., 2013. Volatile, isotope, and organic analysis of martian fines with the Mars Curiosity Rover. Science 341. UNSP 1238937 doi: 10.1126/science.1238937.

Ling, Z.C., Wang, A., 2010. A systematic spectroscopic study of eight hydrous ferric sulfates relevant to Mars. Icarus 209, 422–433. doi:10.1016/j.icarus.2010.05.009.

Lu, Y., Wang, A., 2013. Stability and phase transition pathways of OH-bearing ferric sulfates under the conditions relevant to diurnal, seasonal, and obliquity cycles on Mars. Presented at the 44th Lunar and Planetary Science Conference Abstract #2634.

McAdam, A.C., et al., 2014. Sulfur-bearing phases detected by evolved gas analysis of the Rocknest aeolian deposit, Gale Crater, Mars: Rockness sulfur phases detected by SAM. J. Geophys. Res. Planets 119, 373–393. doi:10.1002/2013JE004518.

McEwen, A.S., et al., 2011. Seasonal flows on warm martian slopes. Science 333, 740–743. doi:10.1126/science.1204816.

Milliken, R.E., Bish, D.L., 2014. Distinguishing hisingerite from other clays and its importance for Mars. Presented at the 45th Lunar and Planetary Science Conference Abstract #2251.

Morris, R.V., et al., 2013. The amorphous component in martian basaltic soil in global perspective from MSL and MER missions. Presented at the 44th Lunar and Planetary Science Conference Abstract #1653.

Morris, R.V., et al., 2015a. Update on the chemical composition of crystalline, smectite, and amorphous components for Rocknest Soil and John Klein and Cumberland Mudstone Drill Fines at Gale Crater, Mars. Presented at the 46th Lunar and Planetary Science Conference. Lunar and Planetary Institute, Houston, p. Abstract #2622.

Morris, R.V., Rampe, E.B., Graff, T.G., Archer, P.D.J., Le, L., Ming, D.W., Sutter, B., 2015b. Transmission X-ray diffraction (XRD) patterns relevant to the MSL CheMin amorphous component: sulfates and silicates. Presented at the 46th Lunar and Planetary Science Conference, Lunar and Planetary Institute, Houston, Abstract #2434.

Morris, R.V., et al., 2016. Silicic volcanism on Mars evidenced by tridymite in high-SiO_2 sedimentary rock at Gale crater. Proc. Natl. Acad. Sci. U.S.A. 113, 7071–7076. doi:10.1073/pnas.1607098113.

Nuding, D.L., Rivera-Valentin, E.G., Davis, R.D., Gough, R.V., Chevrier, V.F., Tolbert, M.A., 2014. Deliquescence and efflorescence of calcium perchlorate: an investigation of stable aqueous solutions relevant to Mars. Icarus 243, 420–428. doi:10.1016/j.icarus.2014.08.036.

Ojha, L., Wilhelm, M.B., Murchie, S.L., McEwen, A.S., Wray, J.J., Hanley, J., Masse, M., Chojnacki, M., 2015. Spectral evidence for hydrated salts in recurring slope lineae on Mars. Nat. Geosci. 8, 829–832. doi:10.1038/NGEO2546.

Osterloo, M.M., Hamilton, V.E., Bandfield, J.L., Glotch, T.D., Baldridge, A.M., Christensen, P.R., Tornabene, L.L., Anderson, F.S., 2008. Chloride-bearing materials in the southern highlands of Mars. Science 319, 1651–1654. doi:10.1126/science.1150690.

Rampe, E.B., et al., 2017. Mineralogy of an ancient lacustrine mudstone succession from the Murray formation, Gale crater, Mars. Earth Planet. Sci. Lett. 471, 172–185. doi:10.1016/j.epsl.2017.04.021.

Rampe, E.B., Morris, R.V., Archer, P.D., Agresti, D.G., Ming, D.W., 2016. Recognizing sulfate and phosphate complexes chemisorbed onto nanophase weathering products on Mars using in-situ and remote observations. Am. Mineral. 101, 678–689. doi:10.2138/am-2016-5408CCBYNCND.

Rogers, A.D., Gregerson, J., Sklute, E.C., Rucks, M., Jensen, H.B., Reeder, R.J., Dyar, M.D., 2016. Sequestration of mixed salts in the amorphous soil fraction on Mars. Presented at the 47th Lunar and Planetary Science Conference Abstract #1736.

Savijarvi, H., 1995. Mars boundary-layer modeling - Diurnal moisture cycle and soil properties at the Viking–Lander-1 Site. Icarus 117, 120–127. doi:10.1006/icar.1995.1146.

Sklute, E.C., Jensen, H.B., Rogers, A.D., Reeder, R.J., 2015. Morphological, structural, and spectral characteristics of amorphous iron sulfates: spectral study of amorphous Fe sulfates. J. Geophys. Res. Planets. 120, 809–830. doi:10.1002/2014JE004784.

Sklute, E.C., Kashyap, A., Dyar, M.D., Holden, J.F., Tague, T., Wang, P., Jaret, S.J., 2017. Spectral and morphological characteristics of synthetic nanophase iron (oxyhydr)oxides. Phys. Chem. Mineral doi:10.1007/s00269-017-0897-y.

Spanovich, N., Smith, M.D., Smith, P.H., Wolff, M.J., Christensent, P.R., Squyres, S.W., 2006. Surface and near-surface atmospheric temperatures for the Mars Exploration Rover landing sites, Icarus, 180, 314–320. doi: 10.1016/j.icarus.2005.09.014.

Toner, J.D., Catling, D.C., Light, B., 2014. The formation of supercooled brines, viscous liquids, and low-temperature perchlorate glasses in aqueous solutions relevant to Mars. Icarus 233, 36–47. doi:10.1016/j.icarus.2014.01.018.

Treiman, A.H., et al., 2016. Mineralogy, provenance, and diagenesis of a potassic basaltic sandstone on Mars: CheMin X-ray diffraction of the Windjana sample (Kimberley area, Gale Crater): CHEMIN: WINDJANA. J. Geophys. Res. Planets 121, 75–106. doi:10.1002/2015JE004932.

Vaniman, D.T., Bish, D.L., Chipera, S.J., Fialips, C.I., Carey, J.W., Feldman, W.C., 2004. Magnesium sulphate salts and the history of water on Mars. Nature 431, 663–665. doi:10.1038/nature02973.

Wang, A., Freeman, J.J., Jolliff, B.L., 2009. Phase transition pathways of the hydrates of magnesium sulfate in the temperature range 50 degrees C to 5 degrees C: implication for sulfates on Mars. J. Geophys. Res.-Planets 114, E04010. doi:10.1029/2008JE003266.

Wang, A., Feldman, W.C., Mellon, M.T., Zheng, M., 2013. The preservation of subsurface sulfates with mid-to-high degree of hydration in equatorial regions on Mars. Icarus 226, 980–991. doi:10.1016/j.icarus.2013.07.020.

Wang, A., Freeman, J.F., Jolliff, B.L., Arvidson, R.E., 2006. Conversion of crystalline $MgSO_4.XH_2O$ to the hydrated amorphous phase – A Raman, NIR, and XRD study. Presented at the 37th Lunar and Planetary Science Conference Abstract #2168.

Wang, A., Freeman, J.J., Chou, I.-M., Jolliff, B.L., 2011. Stability of Mg-sulfates at−10 degrees C and the rates of dehydration/rehydration processes under conditions relevant to Mars. J. Geophys. Res. Planets 116, E12006. doi:10.1029/2011JE003818.

Wang, A., Ling, Z., Freeman, J.J., Kong, W., 2012. Stability field and phase transition pathways of hydrous ferric sulfates in the temperature range 50 °C to 5 °C: Implication for martian ferric sulfates. Icarus 218, 622–643. doi:10.1016/j.icarus.2012.01.003.

Xu, W., Parise, J.B., 2012. Temperature and humidity effects on ferric sulfate stability and phase transformation. Am. Mineral. 97, 378–383. doi:10.2138/am.2012.3927.

Xu, W., Tosca, N.J., McLennan, S.M., Parise, J.B., 2009. Humidity-induced phase transitions of ferric sulfate minerals studied by in situ and ex situ X-ray diffraction. Am. Mineral. 94, 1629–1637. doi:10.2138/am.2009.3182.

Yen, A.S., et al., 2017. Multiple stages of aqueous alteration along fractures in mudstone and sandstone strata in Gale Crater, Mars. Earth Planet. Sci. Lett. 471, 186–198.